Stall detection on a leading-edge plasma actuated pitching airfoil utilizing onboard measurement

Patrick Bowles[*] , Thomas Corke[†] and Eric Matlis[‡]

Center for Flow Physics and Control (FlowPAC), University of Notre Dame, Notre Dame, IN, 46556, U.S.A.

I.   Introduction

DYnamic stall forces helicopter rotor-blades to function at conditions below their mechanical ability, limiting top speed, maneuverability, and loading. Improved and higher performance rotocraft in both military and commercial sectors require advances in rotor/rotor-blade technology. The current research focuses on experimental work to develop a reliable and robust dynamic stall detection and active control scheme to extend rotocraft utility.

At a critical angle of attack, the flow around a static airfoil separates, causing the airfoil to stall. The stall of a rapidly pitching airfoil, conversely, is delayed to higher angles of attack.[1] Due to a large difference in relative speeds, a helicopter's retreating rotor-blade operates at angles of attack significantly greater than the angle of attack of the advancing blade, balancing the lift force on each side of the vehicle. At key forward flight speeds, the retreating blade dynamically stalls, creating an imbalanced lift and forcing the helicopter to roll. The problem is classically known as Retreating Blade Stall (RBS), see Fig. 1, and is attributable to the cyclic nature of the blade. The variable pitch angle provokes the formation of a leading edge or dynamic stall vortex.[1] The vortex increases lift as it propagates over the suction side of the airfoil, but triggers an abrupt loss in lift and nose-down pitching moment after it sheds from the trailing edge, see Fig. 2.[2,3] The influence of the blade wake, blade flapping, and the inconstant pitch of the airfoil creates a time-dependent environment, in which the airfoil may or may not be stalled, suggesting that an active, closed-loop control scheme require on-blade flow sensing mechanisms.
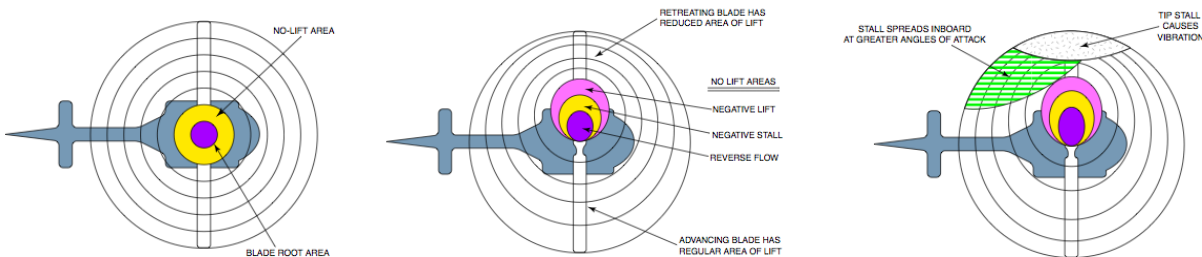

Figure 1. Lift pattern of a helicopter for hover, cruise, and critical forward flight speeds

In an effort to mimic the operating conditions of a helicopter rotor-blade and as a first-step towards active, closed loop control, a commercial servo motor dynamically pitched a cantilevered NACA 0015 airfoil with a reduced frequency of 0.16 and chord based Reynolds number of 86,000. The 0015 statically stalls near an angle of attack of 14°, full, dynamic stall occurs near 25°; separation occurs anytime the airfoil changes from pitch-up to pitch-down. Extensive work has been done in determining separation for a pitching airfoil[4]

---

[*]Graduate Research Assistant, AIAA Student Member

[†]Clark Chair Professor, Associate Fellow AIAA

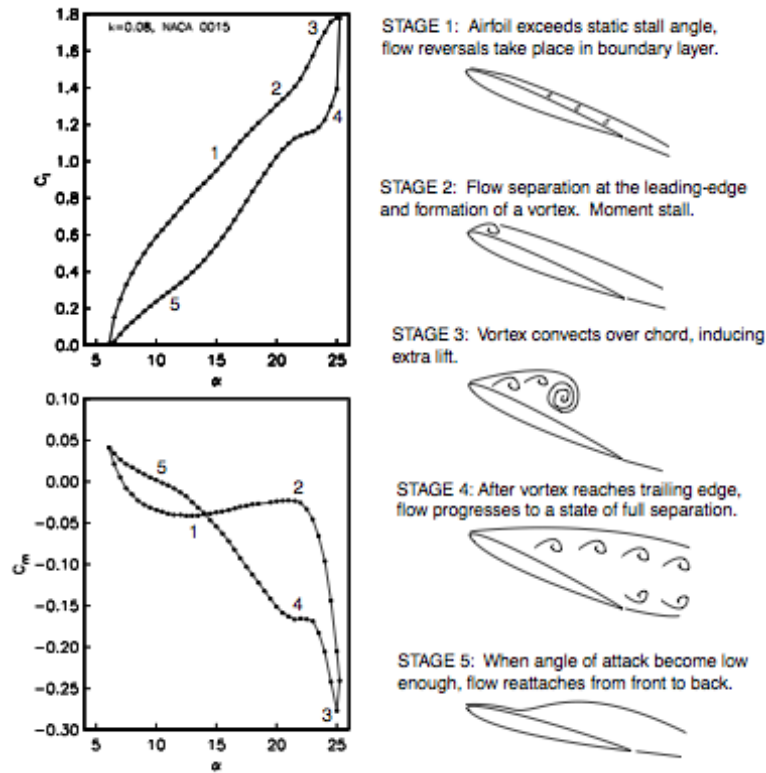[‡]Post-doctoral Research Assistant, Member AIAA

Figure 2. Schematic illustrating flow, lift force, and moment behavior during dynamic stall for a pitching airfoil

and varying approaches exist towards controlling dynamic stall.[5–9] Post[10] utilized single dielectric barrier discharge (SDBD) plasma actuators, flow control devices capable of effectively manipulating natural flow states,[10–14] and a closed-loop scheme,[3] in which the actuators were turned off and on during distinct, pre-defined segments of the pitch-cycle to improve the airfoil's cycle-integrated lift. The current work, on the other hand, employs an in-situ flow sensor to detect separation. The suction side of the airfoil was equipped with a small, immobile, high band-width pressure transducer near a tenth of its chord. An "unsteady" SDBD plasma actuator mounted on the leading edge controlled the flow over the airfoil. The actuator was aligned in the spanwise direction, effectively mixing high momentum fluid outside the boundary layer with low momentum fluid near the airfoil surface, delaying separation. At low angles of attack, periodic disturbances produced by the actuator at a given unsteady actuator frequency are weakened by the strong, favorable pressure gradient over the suction side of the airfoil. Hence, the pressure sensor fails to detect the small-scale disturbances produced by the actuator. As the angle of attack increases, a separation bubble forms,[2] marking the transition from an attached, laminar boundary layer, to an attached, turbulent boundary layer. A transient pressure field replaces the favorable pressure gradient, and the unsteady excitation frequency and associated disturbances become the dominant flow feature at the airfoil's surface, see Fig. 3. The chordwise location of the pressure sensor dictates the angle of attack at which the sensor becomes receptive to imminent flow separation at the leading edge, serving as a "stall" margin.

The airfoil's angular position was given by $\bar{\alpha}+R\sin(2\pi ft)$, where the effects of $\bar{\alpha}$, the mean angle of attack, and R, the amplitude, on the pressure signal were investigated for both uncontrolled and controlled configurations. $\bar{\alpha}$, R, and k are the most significant factors governing dynamic stall.[1] Selection of $\bar{\alpha}$ and R placed the airfoil in varying dynamic stall regimes. Spectrograms and Wavelet Transforms revealed the time-frequency behavior of the signal, and, in conjunction with the Amplitude Peak Sense and Control method (APSC),[12] previously developed to determine separation on a static airfoil, discerned when the flow was separated. Several cases are compared to show the robustness of the separation detection scheme employed.

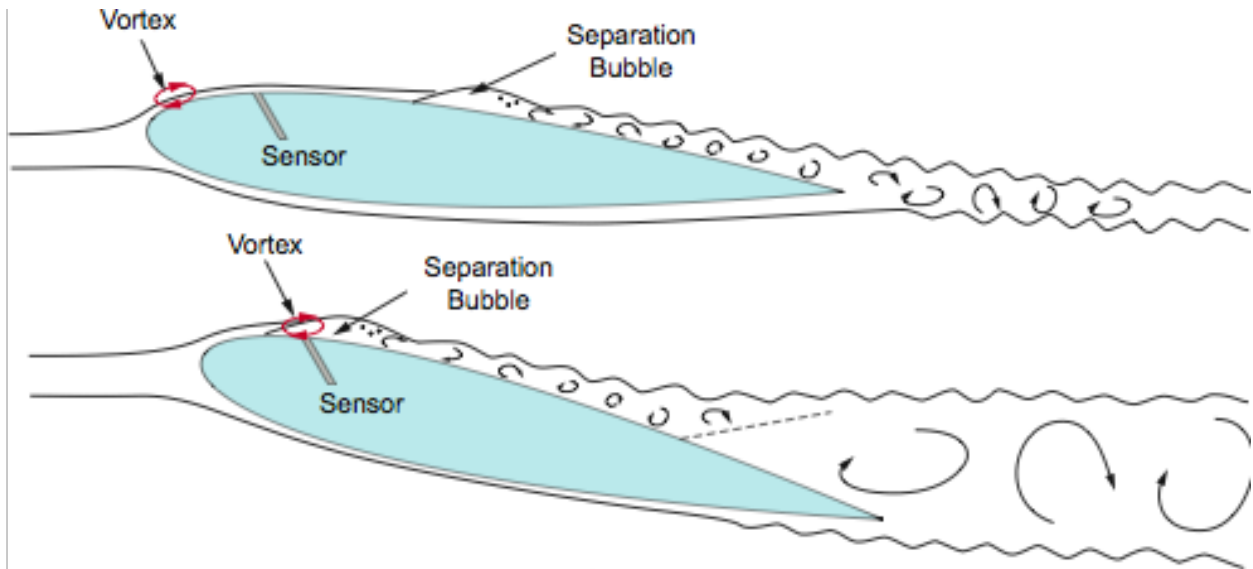American Institute of Aeronautics and Astronautics

Figure 3. Schematic of flow topology around an airfoil at pre-stall and near-stall angles of attack to illustrate the coupling of the plasma actuator and sensor in detecting separation.

II. Experimental Setup

The research was performed in an open-return, subsonic wind tunnel at Hessert Laboratory at the University of Notre Dame. The test section measures 0.61 m × 0.61 m × 1.8 m with a plexiglas front and bottom for both monitoring and flow visualization. The tunnel possesses a removable inlet utilizing twelve screens with an 18:1 contraction ratio. All electronics were located outside but near the test section. A schematic of the test facility is shown in Fig. 4.
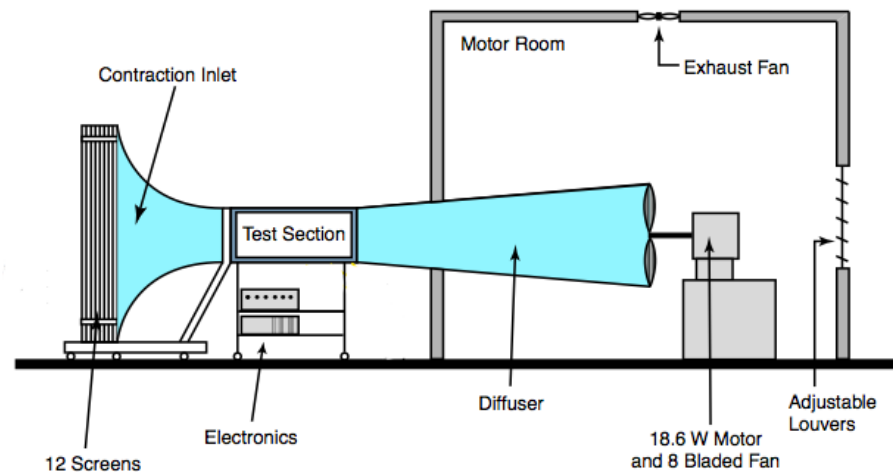

Figure 4. Schematic of test facility

A stand for the servo motor, an Animatics Smart Motor SM3430, and gear box was rigged to the back of the test section. The NACA 0015 airfoil was mounted on a rod, fed through the back wall of the test section with a tube and bearing , and cantilevered to the gear box with an aluminum connection.

The airfoil was cast in a two-part epoxy from a two-peice, numerically machined, aluminum mold. The

American Institute of Aeronautics and Astronautics

airfoil had a 12.7 cm chord and 25.4 cm span. Two, clear plexiglas endplates fastened to the NACA 0015 sides minimized 3-D effects. The end plates measured 40.6 cm × 20.2 cm × 3.2 mm with a radius of 10.2 cm. A slot was milled for an Omega PX72-0.3GV pressure transducer on the pressure side of the airfoil. Tygon tubing connected the suction side pressure port, located at x/c=0.08, where c is the chord length and x the ordinate in the chord-wise direction, to the transducer. The tubing remained stationary at all times.

Each experiment ran at a freestream speed, U_∞, of 10 m/s. The airfoil pitched at a rate, f, of 4 Hz about its quarter chord. The servo motor translated a 0-5 V sine input from a Stanford Research function generator to the desired motion, given by the equation,

$$\alpha = \bar{\alpha} + R sin(2\pi f t) \tag{1}$$

where α is the angular position of the airfoil in degrees. $\bar{\alpha}$ and R were varied using the Smart Motor Interface software accompanying the motor. The reduced frequency, defined as

$$k = \frac{\pi f c}{U_\infty} \tag{2}$$

was 0.16[a]. The Reynold's Number, defined as

$$Re = \frac{U_\infty c}{\nu} \tag{3}$$

was 86,000.

III. Flow Control Technique

THe plasma actuators consisted of two thin electrodes disjoined by a dielectric. The dielectric insulates the bottom electrode, but leaves the top electrode exposed to air. The high voltage, a.c. signal supplied to the electrodes ionized the air along the edge of the exposed electrode, directly over the insulated electrode; the continuous stripping and placement of electrodes from and onto the dielectric surface during each cycle of the a.c. signal generates a body force in the direction of the insulated electrode.

The covered electrode used in the present study was constructed from 0.025 mm copper tape and bonded to the surface of the airfoil. The dielectric was a composite - 0.25 mm Kapton tape and 0.1 mm Teflon tape - and, in that order, was laminated over the bottom electrode. 0.025 mm copper tape was used for the uncovered electrode. See Fig. 5 for a schematic and experimental configuration. The peak-to-peak voltage, V_{pp}, supplied to the actuator was 6.8 kV at a frequency of 5 kHz. F^+ for all data presented was 80 Hz.
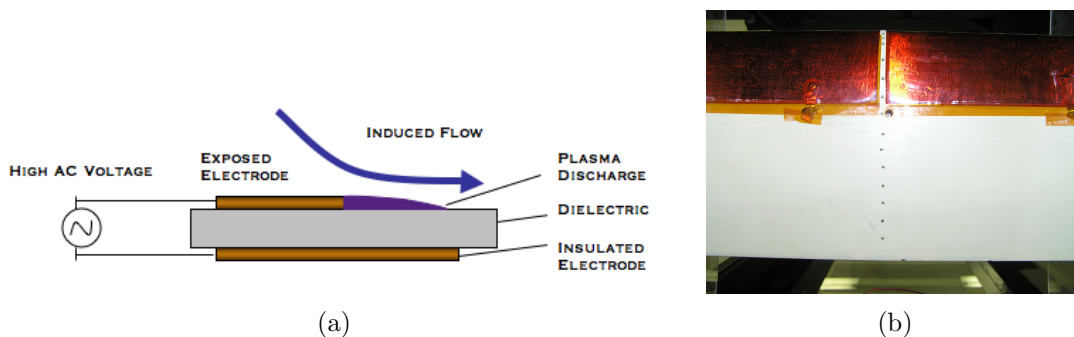

Figure 5. (a)Schematic of plasma actuator. (b) NACA 0015 outfitted with leading edge, spanwise oriented plasma actuators.

IV. Data acquisition

Two signals were acquired in the experiment - the angular position of the airfoil and the pressure signal. An optical encoder installed on the servo motor output the angular position of the motor shaft in two square waves in quadrature. A quadrature decoder, digital to analog converter, and accompanying circuitry

---

[a]Post used the same operating conditions but defined k as half its current value

produced the instantaneous position, α, as an analog voltage. The pressure signal was low-pass filtered at 100 Hz. A digital, low-pass filter was applied to α in postprocessing. A United Electronics Industries (UEI) *PowerDAQ* data acquisition board acquired both analog signals at the sampling rate, F_s, of 2^{16} Hz, for one second (four pitching cycles).

V. Data analysis

SPectograms and discrete Wavelet Transformations mapped the pressure signal's time domain to a 2-D, time-frequency representation. Analogous to the Heisenberg Uncertainty Principle in quantum mechanics, the absolute frequency of the signal cannot be known at a given time; conversely, the absolute time a measured frequency occurs remains uncertain.[15] Conventional frequency mappings, such as Fourier transforms (FT), were ignored due to the loss of temporal information and subsequent failure to illustrate how the separation detection mechanism functions.

V.A. The Short-Time Fourier Transform (STFT)

The Gabor transform or STFT translates an analysis window, the "windowing function", along the signal, capturing changes in the spectral content of the signal as a function of time using the trigonometrically based FT . The continuous STFT[15–17] is defined

$$G(\tau, \omega) = \int_{-\infty}^{\infty} F(t)g(t - \tau)e^{-i\omega t}dt \tag{4}$$

where G is the time-frequency coefficient matrix of the mapped signal F(t), g is the user-defined windowing function - a Hanning function in this application - τ is the time marching increment determined by the size (length) of g, and ω represents frequency in rad/s. The discrete implementation is defined

$$G(m, \omega) = \sum_{n=-\infty}^{\infty} F[n]g[n - m]e^{-i\omega n} \tag{5}$$

where n designates the index of the signal associated with t and, likewise, m the index associated with τ. The squared norm of G, $|G|^2$ is called a spectrogram. G restricts the FT of F to the vicinity of t=b by computing the FT of the product of F and g. g must meet several criteria.[15] The length of g rigidly fixes the temporal and spectral resolution of the transform, making it difficult for the STFT to analyze rapidly varying signals.[17]

In processing the pressure signal, the original signal of length $N = 2^{16}$ discrete points, was decimated to a length of N=2^{10} reducing the effective F_s from 2^{16} to 2^{10} and providing a frequency resolution, defined as

$$\hat{f} = \frac{F_s}{N} \tag{6}$$

of 1 Hz. The length of the Hanning window transformed the N time indices to m= 241 short-time indices. The maximum frequency analyzed was set to 120Hz, slightly above the low-pass cutoff frequency to ensure that no physical frequencies left in the signal were discarded. Two main frequencies of interest exist in this application, F^+= 80 Hz and f= 4 Hz. The choice of the length of g requires a compromise in spectral and frequency resolution capable of adequately resolving the two frequencies. However, due to a lack of frequency resolution, the spectrogram shows difficulty in distinguishing the the 4 Hz pressure variation.

V.B. The Wavelet Transform : Mexican Hat

Unlike the STFT, the wavelet transform[15–18] smartly performs mutli-resolution analysis, making it capable of discerning both F* and f. The analysis window or mother wavelet, ψ, translates and dilates: it widens in time to capture the slow, low-frequency content of the signal, and collapses in time to encapsulate fast, high frequency components. The review article by Farge[18] provides a thorough treatise of wavelets from a fluid perspective.

The continuous wavelet transform is defined

$$W_\Psi(\tau, a) = \frac{1}{\sqrt{|a|}} \int_{-\infty}^{\infty} F(t)\Psi\left(\frac{t - \tau}{a}\right) dt \tag{7}$$

American Institute of Aeronautics and Astronautics

where a, the scale or dilation factor, is inversely proportional to frequency, and τ translates Ψ in time. The discrete implementation is defined

$$W_\Psi(n, a) = \sum_{n=-\infty}^{\infty} F(n)\Psi\left(\frac{n-m}{a}\right).$$ (8)

The Mexican Hat wavelet transform was applied to the pressure transducer signal. The Mexican Hat is the Laplacian of the Gauss distribution, its normalized version is defined as

$$\Psi = \frac{1}{\sqrt{2\pi a^3}}\left(1 - \frac{t^2}{a^2}\right)e^{-t^2/2a^2}.$$ (9)

The Mexican hat was used to better resolve both the temporal information near the unsteady actuator frequency and the fundamental, 4 Hz frequency resulting from the pitch-rate of the airfoil. In conjunction, the spectrogram and wavelet mappings yield a confident, time-frequency interpretation of the pressure signal's transient and physical behavior.

VI. Results and Discussion

Results are presented for five select cases and fall into three, varying dynamic stall regimes, from no stall to deep stall in accordance with McCroskey.[1] The maximum angle of attack, $\alpha_{max} = \bar{\alpha} + R$, defines the most important factor in dictating the stall regime. The spectrogram and wavelet coefficients of the pressure transducer signal are presented for each case. Graphs (a) and (d) in Fig. 7-12 show non-dimensional pressure, P* and non-dimensional position, α^* defined by

$$P^* = \frac{P - \bar{P}}{||P||_1}$$ (10)

$$\alpha^* = \frac{\alpha - \bar{\alpha}}{||\alpha||_1}$$ (11)

where an over-bar represents the mean. Obviously, α^*=sin(2π ft-ϕ) where ϕ is the phase of the signal associated with the data acquisition's start. Since α^* deviates from the desired position, a "perfect" trajectory is provided on graphs (a) and (d) in Fig. 7-12 for reference. Fig. 6 illustrates the angular position of the airfoil and how the flow and pressure data corresponds to position. The flow behavior, with labels (1)-(5), complies with the descriptions provided in Fig. 3 . A general inquiry of Fig. 7-12 assures the reader that, as expected, pitch-down [Fig. 6, (5)] results in a suction-side pressure increase and pitch-up [Fig. 6, (2)] yields a suction-side pressure decrease.
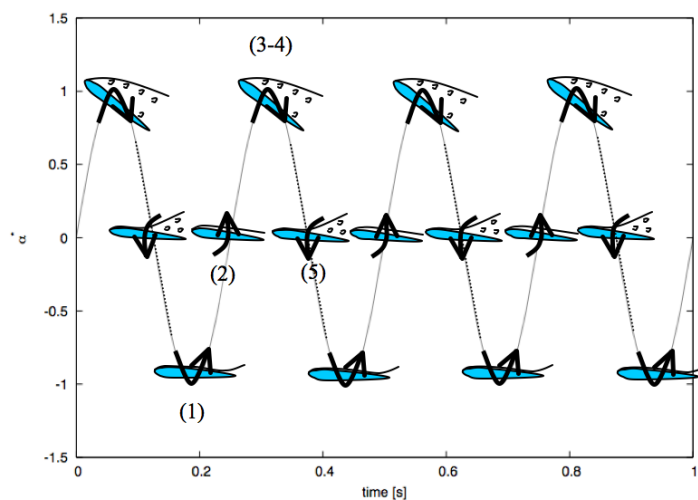

Figure 6. Schematic of airfoil motion, $\alpha^* = sin(2\pi ft)$ and associated flow topology for analyzing pressure data. Dotted lines, (5) signify portions of the pitch-cycle where the flow is likely to be separated.

American Institute of Aeronautics and Astronautics

VI.A.   No Stall : $\alpha_{max} = 10^o$

The no stall case is shown in Fig. 7. Nominal separation distinguishes the category, indicated by the lack of higher frequency content in the pressure signal in both the spectrogram and wavelet coefficients, including position (3-4) in (b) and (c). The dominant frequency, f=4 Hz, stems from the airfoil's periodic motion for both the uncontrolled and controlled cases. The pressure signal behaves as a near perfect sinusoid in (a). In (b), the pressure fluctuates when the airfoil changes from pitch-up to pitch-down, (3-4), at a frequency near F^+ realized in (e) as small "blobs", a result of partial, momentary separation from the change in direction; however, the actuated spectrogram coefficients are small and the wavelet coefficients in (f) near F^+ are negligible, suggesting that the actuators had little effect on the flow field through the range of motion. The 4 Hz frequency band of wavelet coefficients in (c) and (f) appear nearly identical.
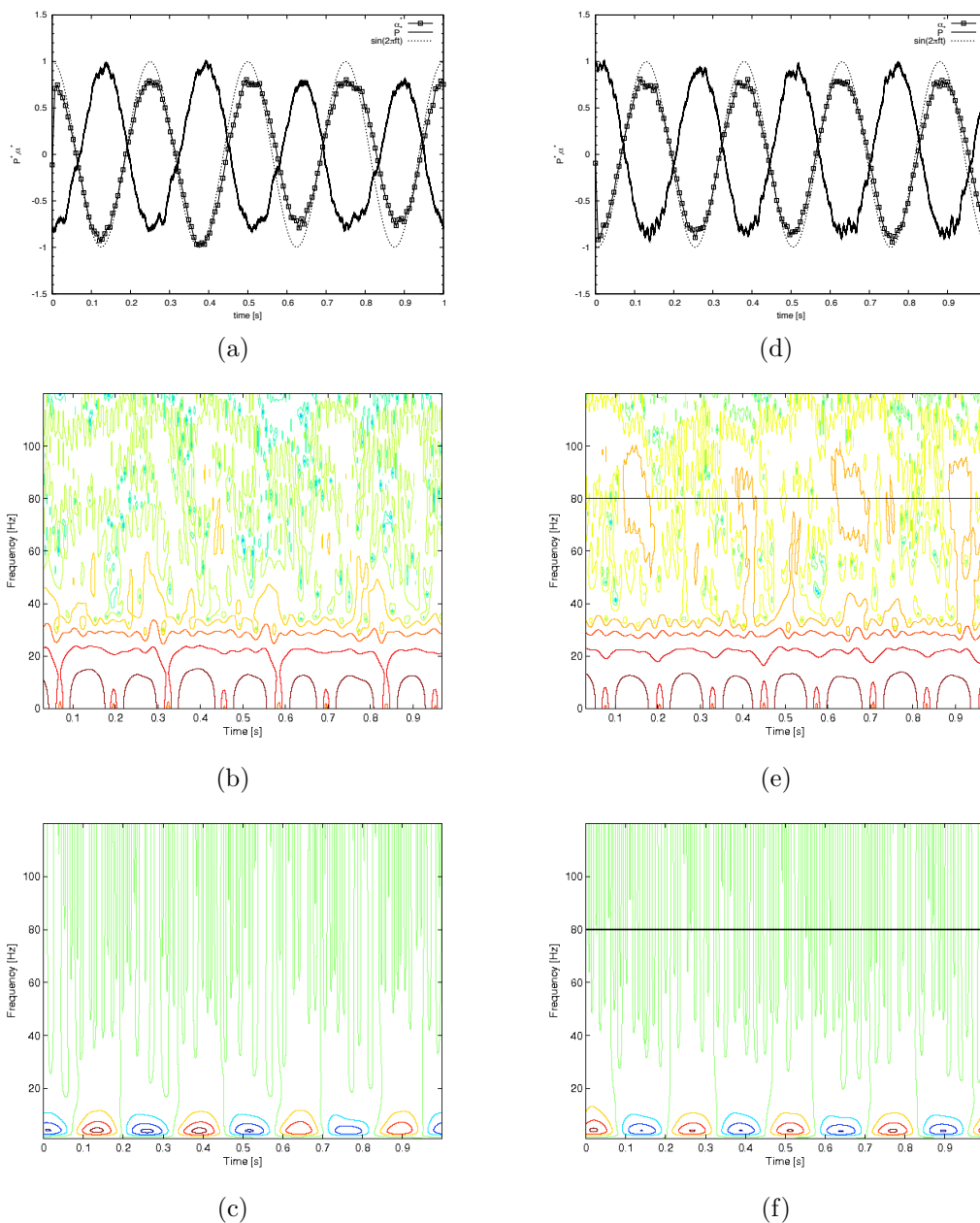

Figure 7. Time and time-frequency representations of the pressure signal for $\bar{\alpha} = 5^o$, $R = 5^o$. (a)-(c): No acuation. (d)-(f): $F^+ = 80$ Hz. (a)&(d) Position and pressure time traces. (b)&(e) Spectrogram of pressure signal. (c)&(f) Mexican Hat Wavelet coefficients.

American Institute of Aeronautics and Astronautics

VI.B. Light Stall: $\alpha_{max} = 15^o$ and 16°

The pressure signal in Fig. 8 (a) and (d) show drastically different characteristics compared to Fig. 7; pure sinusoidal behavior is absent, illustrated by the "warped" peaks near 4Hz in (c). The pressure signal leads the angular position in (a), as the formation of the LEV quickens the pressure drop during pitch-up. Small variations in P* of (a) yield spectral content at frequencies greater than 4Hz in (b) and (c). Translation of a small, DSV over the suction side of the airfoil accounts for the local maxima at (3-4) in (a), exhibited by the last three cycles. Plasma actuation instills its signature during segment (5) of α^*, seen clearly in (d) and visualized again as "blobs" in (e). Further, (d) shows that the pressure fails to lead position. Streaks near F^+ appear in (f), but the associated wavelet coefficients remain small. Disregarding the modulated unsteady actuator frequency in (d), the pressure signal varies more sinusoidally than in (a). Fig. 8 (e) confirms this conclusion as the 4 Hz band of wavelet coefficients closely resemble those of Fig. 7 (c) and (e).
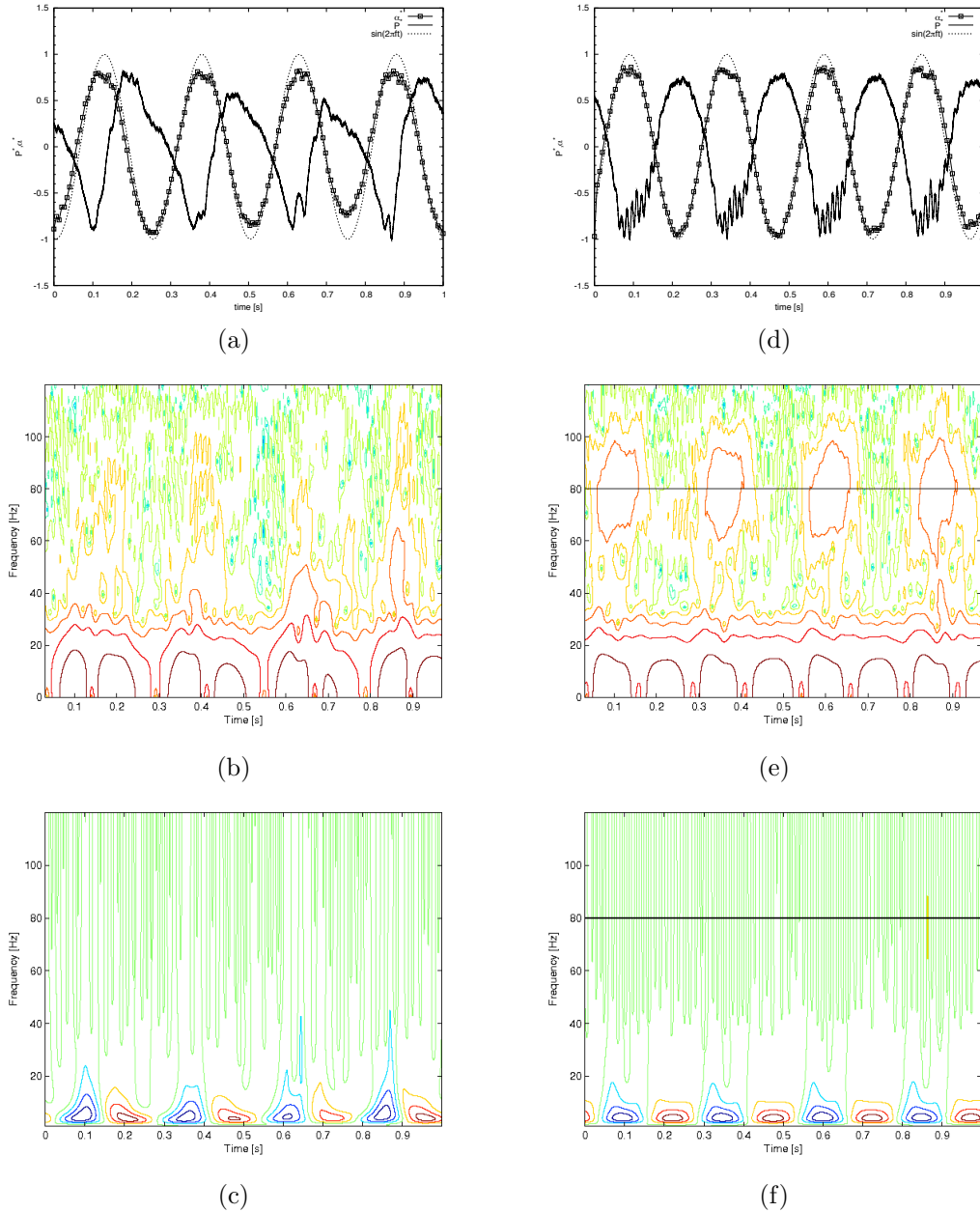

(a)

(d)

(b)

(e)

(c)

(f)

Figure 8. Time and time-frequency representations of the pressure signal for $\bar{\alpha} = 10^o$, $R = 5^o$. (a)-(c): No acuation. (d)-(f): $F^+ = 80$ Hz. (a)&(d) Position and pressure time traces. (b)&(e) Spectrogram of pressure signal. (c)&(f) Mexican Hat Wavelet coefficients.

Fig. 9 shows characteristics similar to Fig. 8 and the same conclusions can be reached by comparison. However, this particular set of data showed no local maxima near (3-4) during each cycle, indicating little DSV interaction. As in Fig. 8, Fig. 9 (d)-(e) illustrate the effectiveness of the separation detection routine, as both the spectrogram and wavelet coefficients show large amplitudes near the band of frequencies centered at 80 Hz. Again, at this angular position, (5), separation is expected. In contrast to Fig. 8 (e), the magnitude of the wavelet coefficients shown in Fig. 9 (e) of P* are significantly larger. The 1° increase of α_{max} caused the pressure signal to level-off in (a), effecting the wavelet coefficients in (c). The actuated airfoil lacks this phenomena and the 4 Hz band of wavelet coefficients in (f) more closely mimic those of Fig. 8 (f).
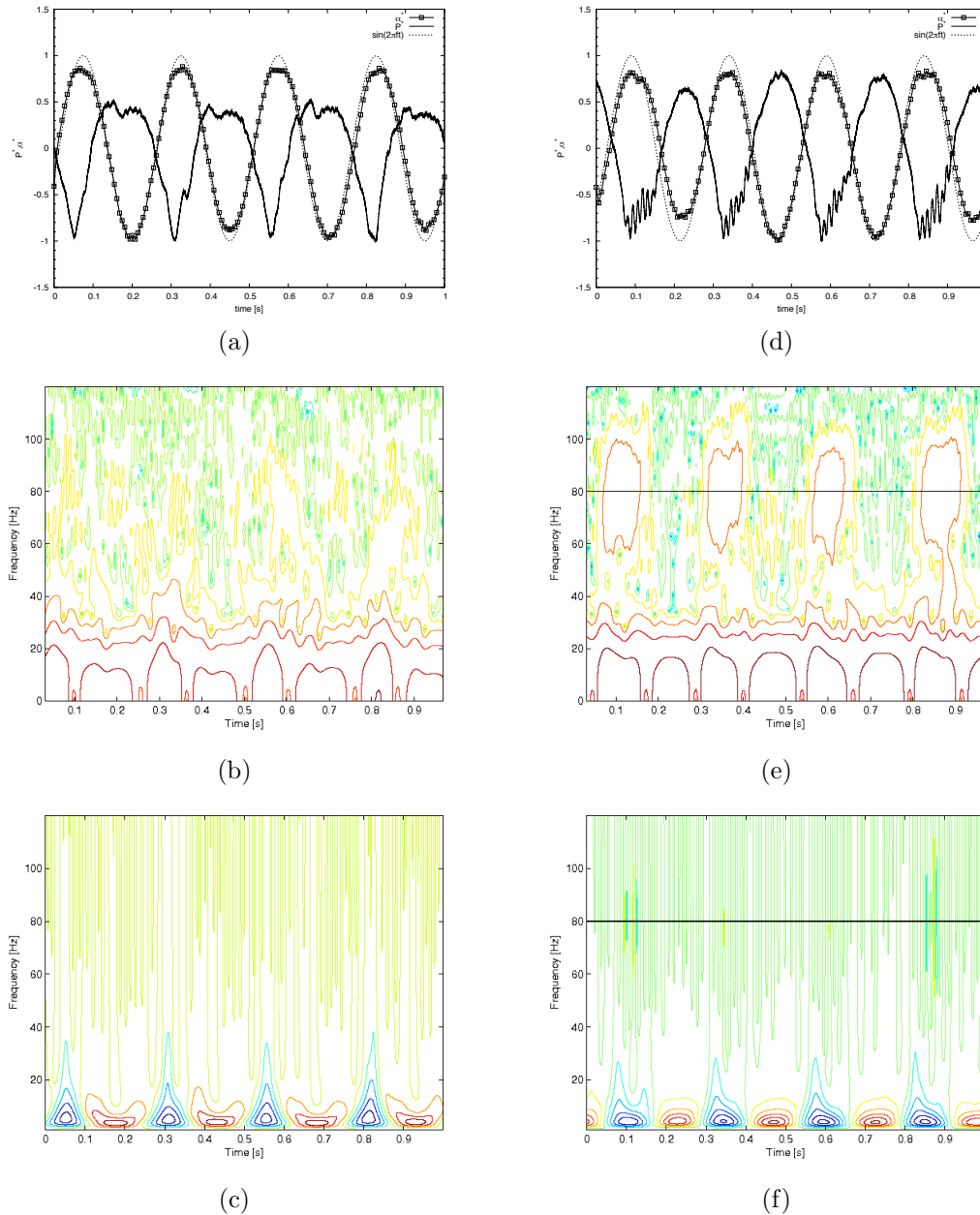

Figure 9. Time and time-frequency representations of the pressure signal for $\bar{\alpha} = 8^o$, $R = 8^o$. (a)-(c): No acuation. (d)-(f): $F^+ = 80$ Hz. (a)&(d) Position and pressure time traces. (b)&(e) Spectrogram of pressure signal. (c)&(f) Mexican Hat Wavelet coefficients.

American Institute of Aeronautics and Astronautics

VI.C. Deep Stall: $\alpha_{max} = 22^o$ and 25°

The formation and propagation of the leading edge vortex over the suction side of the airfoil characterizes deep stall. The pressure signal further leads the angular position due to the vortex. A distinct, local maxima occurs in the motion range (3-4), shown in Fig. 10 (a), indicating that separation occurs at high angles just before transition from pitch-up to pitch-down, (3-4), and is most likely a marker for the propagation of the leading edge vortex over the NACA 0015's suction-side. (c) suggests that the pressure "bump" might have some natural frequency as it appears periodically in the wavelet transform (at a nearly identical frequency range) but is too close to the frequency of motion for the spectrogram in (b) to resolve. Fig. (d) exhibits the influence of the actuator on the pressure signal; P^* plateaus from (3-4) well into (1) and both (e) and (f) show significant spectral content near 80 Hz for the entire stall period. The wavelet coefficients in (e) precisely point out instances in which larger frequencies near 80 Hz are present; the 4 Hz content of the signal lacks the low, natural frequency of (c) and more closely resembles light stall.
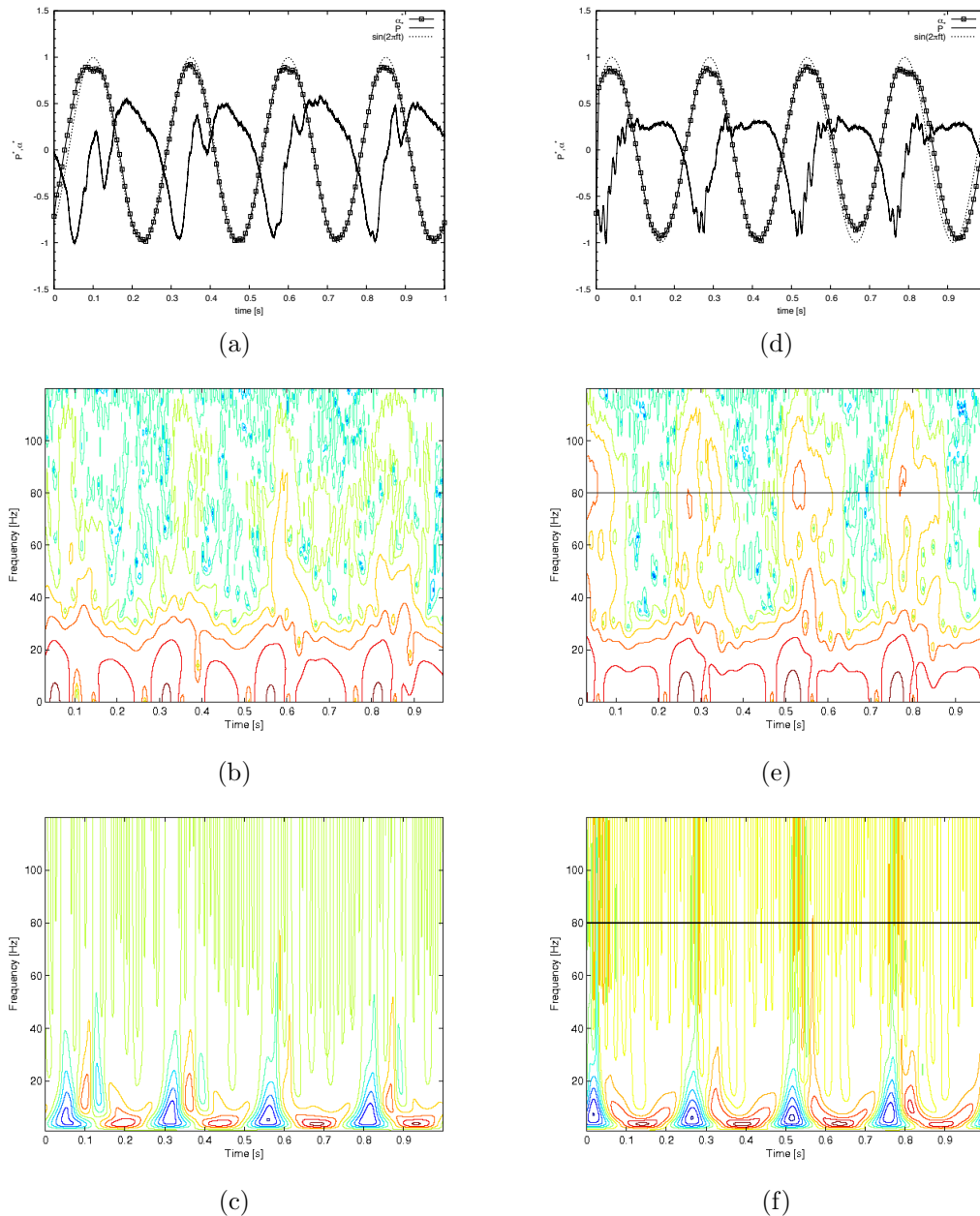

Figure 10. Time and time-frequency representations of the pressure signal for $\bar{\alpha} = 12^o$, $R = 10^o$. (a)-(c): No acuation. (d)-(f): $F^+ = 80$ Hz. (a)&(d) Position and pressure time traces. (b)&(e) Spectrogram of pressure signal. (c)&(f) Mexican Hat Wavelet coefficients.

Fig. 11, despite a three degree increase in α_{max}, behaves similarly to Fig. 10. (a) shows a possible "double" bump or two consecutive local maxima in the first two cycles of the data. (c) shows similar frequencies as Fig. C5 (c) for the peak's natural frequency. Fig. (d) and (e) illustrate the coupling between unsteady actuator frequency and the pressure transducer. However, the peak found in (a) remains in (d), suggesting that the dynamic stall vortex is still present. The 4 Hz band of frequency in the Mexican hat transform for the actuated airfoil mirrors the coefficients found in Fig. 10 (c).
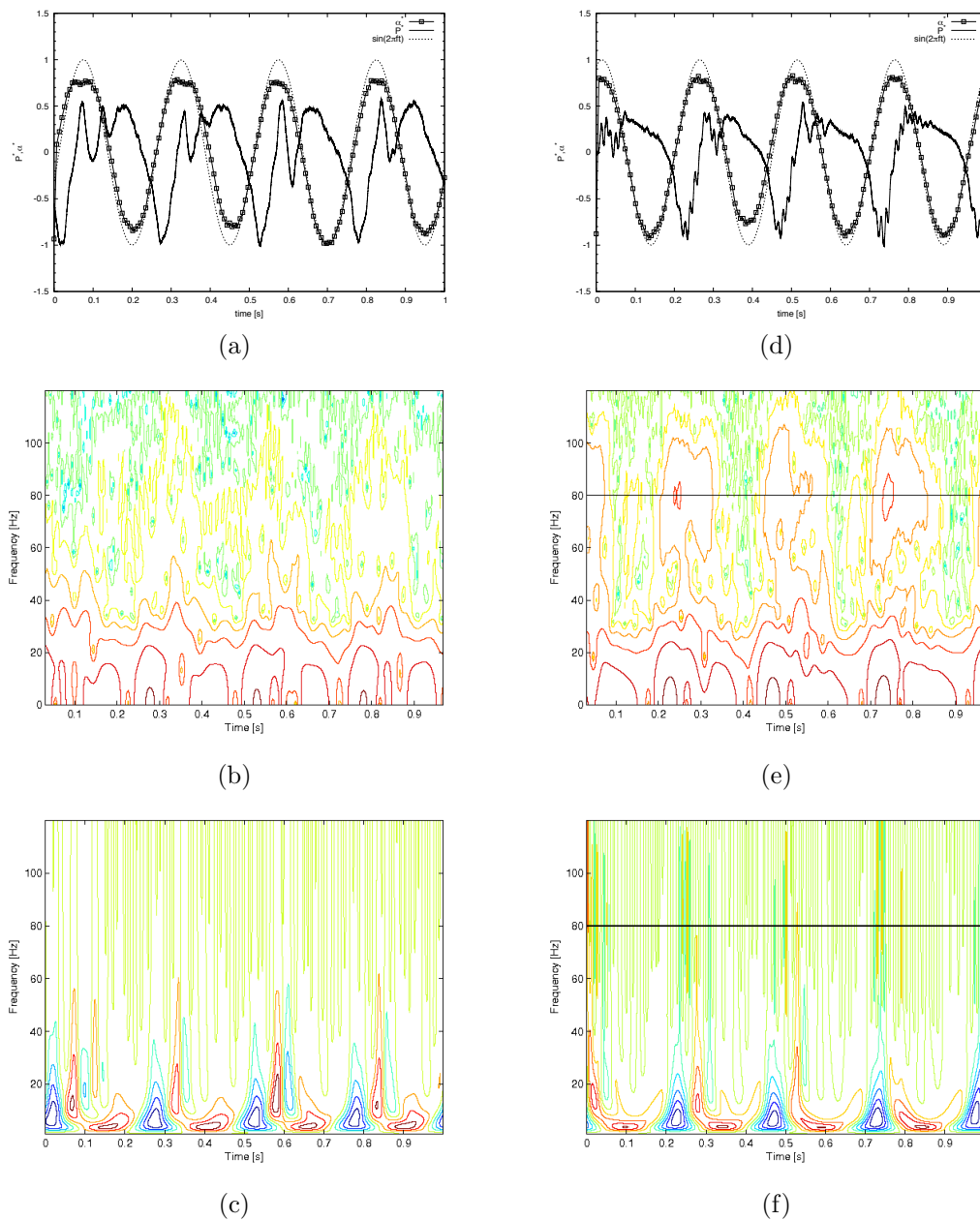

Figure 11. Time and time-frequency representations of the pressure signal for $\bar{\alpha} = 15^o$, $R = 10^o$. (a)-(c): No acuation. (d)-(f): $F^+ = 80$ Hz. (a)&(d) Position and pressure time traces. (b)&(e) Spectrogram of pressure signal. (c)&(f) Mexican Hat Wavelet coefficients.

VII. Conclusion

Plasma actuation at the leading edge of a NACA 0015 airfoil delayed dynamic stall. The current study showed that by coupling the actuator and in-situ pressure sensor, imminent flow separation and stall are detected. This suggests that a real-time RBS sense and control scheme for rotorcraft can be implemented utilizing the APSC method as an indicator function. The unique feature of this approach is that it not only provides a stall pre-cursor than can be used to activate the plasma actuator to control dynamic stall, but also, following stall, can detect when the flow would naturally be attached and the actuator is no longer needed, as quantified by the investigation of light and deep dynamic stall. Future work (closed-loop feedback control) will utilize the APSC method as an indicator to inform a controller when to increase or decrease the power supplied to the actuators from a marginal level to a value capable of controlling dynamic stall in real-time. This separation detection scheme provides robust underlying physics capable of handling any flight condition, thereby increasing the utility and operational envelope of modern rotorcraft.

References

[1] McCroskey, W., "The Phenomenon of Dynamic Stall," Tech. rep., NASA, March 1981.

[2] Leishman, J. G., *Principles of Helicopter Aerodynamics*, Cambridge University Press, 2000.

[3] Post, M. L., *Plasma Actuators for Separation Control On Stationary and Oscillating Airfoils*, Ph.D. thesis, University of Notre Dame, May 2004.

[4] Telionis, D. P., *Unsteady Viscous Flows*, Springer-Verlag, 1981.

[5] Nguyen, K., "Active Control of Helicopter Blade Stall," *Journal of Aircraft*, Vol. 35, 1998.

[6] Post, M. L. and Corke, T. C., "Separation Control Using Plasma Actuators: Dynamic Stall Vortex Control on Oscillating Airfoil," *AIAA Journal*, Vol. 44, 2006.

[7] Kerho, M., "Adaptive Airfoil Dynamic Stall Control," Aerospace Sciences Meeting and Exhibit, AIAA, January 2005.

[8] Singh, C., Peake, D. J., Kokkalis, A., Khodagolian, V., Coton, F. N., and Galbraith, R., "Control of Rotorcraft Retreating Blade Stall Using Air-Jet Vortex Generators," *Journal of Aircraft*, Vol. 43, 2006.

[9] Florea, R. and Wake, B. E., "Parametric Analysis of Directed-Synthetic Jets for Improved Dynamic-Stall Peformance," Aerospace Sciences Meeting and Exhibit, AIAA, 2003.

[10] Corke, T. C. and Post, M. L., "Overview of Plasma Flow Control: Concepts, Optimization, and Applications," *AIAA*, 2004.

[11] Dyken, R. V., McLaughlin, T. E., and Enloe, C. L., "Parametric Investigation of a Single Dielectric Barrier Plasma Actuator," Aerospace Sciences Meeting and Exhibit, AIAA, 2004.

[12] He, C. and Corke, T. C., "Plasma Flaps and Slats: An Application of Weakly-Ionized Plasma Actuators," *AIAA*, 2004, pp. 1–9.

[13] Corke, T. C., Mertz, B., and Patel, M. P., "Plasma Flow Control Optimized Airfoil," *AIAA*, , No. 2006-1208, 2006.

[14] Patel, M. P., Ng, T. T., Vasudevan, S., Corke, T. C., Post, M. L., McLaughlin, T. E., and Suchomel, C. F., "Scaling Effects of an Aerodynamic Plasma Actuator," *Journal of Aircraft*, Vol. 45, 2008, pp. 223–236.

[15] Chui, C. K., *An Introduction to Wavelets*, Vol. 1, Academic Press, 1992.

[16] Stark, H.-G., *Wavelets and Signal Processing*, Springer, 2005.

[17] Williams, W., *Wavelet Trasforms and Time-Frequency Signal Analysis*, Birkhauser, 2001.

[18] Farge, M., "Wavelet Transforms and Their Applications to Turbulence," *Annual Review of Fluid Mechanics*, 1992.